Precise Colloidal Plasmonic Photocatalysts Constructed by Multi-Step Photodepositions

Hyun Dong Ha[1,2†], Chang Yan[1,2†], Georgios Katsoukis[4], Gaurav A. Kamat[3], Ivan A. Moreno-Hernandez[1], Heinz M. Frei[4]*, and A. Paul Alivisatos[1,2,5,6]*

[1]Department of Chemistry, University of California, Berkeley, California 94720, United States

[2]Materials Sciences Division, Lawrence Berkeley National Laboratory, Berkeley, California 94720, United States

[3]Department of Chemical and Biomolecular Engineering, University of California, Berkeley, California 94720, United States

[4]Molecular Biophysics and Integrated Bioimaging Division, Lawrence Berkeley National Laboratory, Berkeley, California 94720, United States

[5]Kavli Energy NanoScience Institute, Berkeley, California 94720, United States

[6]Department of Materials Science and Engineering, University of California, Berkeley, California 94720, United states

* corresponding author, email: paul.alivisatos@berkeley.edu, hmfrei@lbl.gov

[†]These authors contributed equally to this work

(*Nano Lett*., accepted)

Keywords: plasmonic photocatalysis, precise nanostructures, oxygen evolution reaction, photodeposition, Z scheme, Au nanocrystal.

Abstract

Natural photosynthesis relies on a sophisticated charge transfer pathway among multiple components with precise spatial, energetic, and temporal organizations in the aqueous environment. It continues to inspire and challenge the design and fabrication of artificial multi-component colloidal nanostructures for solar-to-fuel conversion. Herein we introduce a plasmonic photocatalyst synthesized with colloidal methods with five integrated components including co-catalysts installed in orthogonal locations. The precise deposition of individual inorganic components on an Au/TiO_2 nanodumbell nanostructure is enabled by photo-reduction and photo-oxidation which selectively occurs at the TiO_2 tip sites and Au lateral sites, respectively. Under visible light irradiation, the photocatalyst exhibited activity of oxygen evolution from water without scavengers. We demonstrate that each component is essential for improving the photocatalytic performance. In addition, mechanistic studies suggest that the photocatalytic reaction requires combining the hot charge carriers derived from exciting both the *d-sp* interband transition and the localized surface plasmon resonance of Au.

Utilizing solar energy to effectively generate renewable fuels is a significant challenge attracting wide scientific attention.[1,2] Both natural and artificial photosynthetic systems typically consist of multiple co-catalysts, charge acceptors, and light absorbers. An efficient design for solar-to-fuel conversion requires precise charge transfer pathways among different components. Such designs with high performance have been realized for lithographically fabricated structures used in photoelectrochemistry (PEC),[3–7] but they face some challenges for scaling to high volumes. Differently, natural photosynthesis machinery built from nanoscale structural units organized in a highly ordered fashion is available on a planetary scale but is still low in power efficiency.[8–10] The bottom-up integration of all the artificial components to create a precise colloidal photosynthesizer remains extremely challenging with the current state of nanoscale synthesis, as it requires stringing together a particularly long series of orthogonal steps involving different inorganic materials.

There has been rapid progress in the synthesis and characterization of a large library of complex nanostructures containing multiple compositions including oxides, semiconductors, and metals.[11–13] For the purpose of promoting photocatalytic reactions, nanostructures with the anisotropic design to collect photo-generated electrons and holes at separated sites are highly desired. Efficient anisotropic photocatalysts with two or three components can be synthesized by leveraging the chemical reactivity of different inorganic components or nanocrystal facets. Some of the most advanced examples include metal-tipped CdS nanorods,[14] CdSe/CdS dot-in-rod structure with metal tips,[15] and Pt-decorated Au/TiO_2 nanodumbells.[16,17] Another fabrication strategy is photochemical deposition which relies on the guided flow of charges in a semiconductor or metal nanocrystal to reduce or oxidize precursors at specific locations of a nanoparticle.[18–20]

Herein, we demonstrate that guided charge flow in the Au/TiO_2 nanodumbell structure can be harnessed to accurately photodeposit multiple inorganic components on either the TiO_2 tips or the lateral sites of the Au nanorod (NR). The plasmonic excitation of Au NR can generate hot electrons to be collected on the TiO_2 tips, leaving holes on the Au NR.[3,16,21] Therefore, the sites of photo-reduction and photo-oxidation become well separated. With all the essential components, including Au, TiO_2,

CoO_x, Pd, and Cr_2O_3, we construct a nanostructure with photocatalytic activity of oxygen evolution reaction (OER) from water without scavengers under visible light solar irradiation. Previously, colloidal plasmonic photocatalysts with fewer components have been shown to achieve hydrogen evolution reaction (HER) with hole scavengers.[22–24] To achieve the more challenging OER reaction without using scavengers, the synthetic problem of integrating more components into a colloidal plasmonic photocatalyst needs to be tackled. This work is inspired by the earlier top-down lithographic work of Moskovits *et al.*,[3] who fabricated a plasmonic PEC device for water splitting by integrating Au, TiO_2, CoO_x and Pt.

Au plasmonic absorbers have many desirable properties for photocatalysis, such as large absorption cross-section, tunable spectrum over the visible wavelengths, and intrinsically high photostability.[25–28] The *d-sp* interband transition and the localized surface plasmon resonance (LSPR) of Au can both provide charge carriers covering a wide range of energies.[29–32] In this work, we suggest that the photocatalytic OER without scavengers in water proceeds by combining the hot charge carriers derived from both the *d-sp* interband transition and the LSPR transition in a pathway resembling the Z-scheme in natural photosynthesis.

The architecture of the photocatalyst with all the integrated components is shown in Fig. 1a. The Au NR harvests photons by LSPR and *d-sp* interband transitions. Titanium dioxide caps on the two tips of the NR form two metal-semiconductor Schottky junctions to intercept the short-lived hot electrons generated from the LSPR modes.[33,34] A thin cobalt oxide (CoO_x) layer on the lateral sites functions as the OER co-catalyst. Palladium nanoparticles on the TiO_2 caps functions as the hydrogen evolution reaction HER co-catalyst. Finally, a thin layer of chromium oxide covers the Pd nanoparticles. The added design of a Cr_2O_3 layer blocks O_2 from reaching the Pd surface, and therefore reduces the oxygen reduction back reaction.[35–37] As shown in Fig. 1b, the deposition of Pd, CoO_x and Cr_2O_3 on Au/TiO_2 nanodumbells is performed by photo-reduction or photo-oxidation of the metal precursor of each component in aqueous solutions under white light LED illumination. The CoO_x was installed by photooxidation of $CoCl_2$ with sodium persulfate as the electron scavenger. The Pd and

Figure 1. a) A schematic illustration of the functional design of the integrated photocatalyst nanoparticle including all the individual components. **b)** The synthetic route with multi-step photodepositions that lead to the precisely integrated photocatalyst. **c)** Normalized absorption spectrum of the integrated photocatalyst.

Cr_2O_3 were installed by photoreduction of H_2PdCl_4 and K_2CrO_4, respectively, using methanol as the hole scavenger. The integrated photocatalyst performs oxidation on the CoO_x sites and reduction on

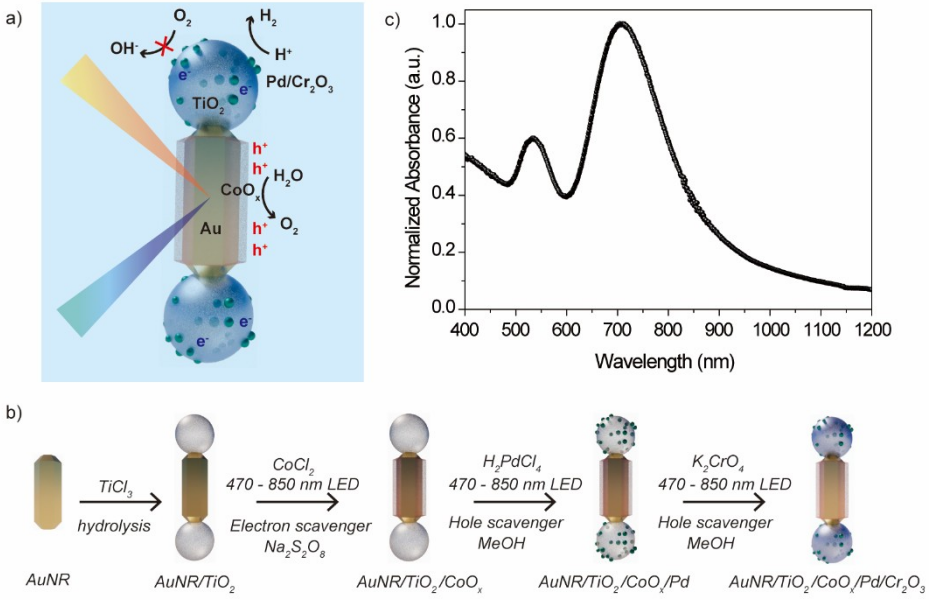

the Pd/Cr_2O_3 sites. This synthetic method does not require selective surface passivation using special surfactant ligands and is generalizable for depositing other metal or oxides.

The absorption spectrum of the integrated photocatalyst is shown in Fig. 1c. The spectrum is very similar to the spectrum of the Au NR at the beginning of the synthetic route, with minor shifts due to the local change of dielectric environments caused by the installation of each inorganic component (Fig. S6). The LSPR band includes a minor transverse mode centered at 533 nm and a major longitudinal mode centered at 705 nm. As the Au/TiO_2 junctions locate at the two tips of the NR, the longitudinal LSPR mode associated with the electron oscillations along the long axis of the NR is expected to play the major role for promoting the electron across the Schottky barrier.[38,39] The sharper LSPR modes are convoluted with the broad *d-sp* interband transition of Au. For photon energy < 2.3 eV (540 nm), the absorption band is mostly attributed to the prominent longitudinal LSPR mode with the tail of *d-sp* interband transition of Au which can extend to around 1.7 eV (730 nm).[40] For photon energy > 2.3 eV, the absorption band is dominated by the *d-sp* interband transition of Au and the transverse LSPR mode.[25,32,41,42] As discussed below, we can analyze the roles played by LSPR and interband transitions in photocatalysis by applying long pass or short pass optical filters.

Transmission electron microscope (TEM) images are displayed in Fig. 2a-2b. The size of the Au NRs was 38±4 nm in diameter and 92±8 nm in length. Under careful examination, a 3-5 nm thin layer of deposits composed of mostly cobalt oxides can be observed coating on the sides of the Au rods (Fig. S4b). The spherical Pd nanoparticles on TiO_2 have a diameter around 5-8 nm. Amorphous Cr_2O_3 are indistinguishable from the underlying TiO_2 due to similar contrast. To characterize the elemental distribution of the multi-component structure, energy dispersive x-ray (EDX) spectral mapping was performed using a scanning transmission electron microscope (STEM) under the high-angle annular dark-field imaging (HAADF) mode. EDX spectra were integrated and compared between the tip region and the central region (Fig. 2c-2e). The Co and Au signals were mostly detected in the central region while the Ti, Cr, and Pd signals were mostly observed in the tip region. The EDX signals of each element were mapped onto the HAADF images of two integrated photocalalyst nanoparticles in Fig. 2f to demonstrate the accomplished site-selective depositions. Mappings were also performed at lower magnifications to confirm the homogeneity of the architecture (Fig. S7).

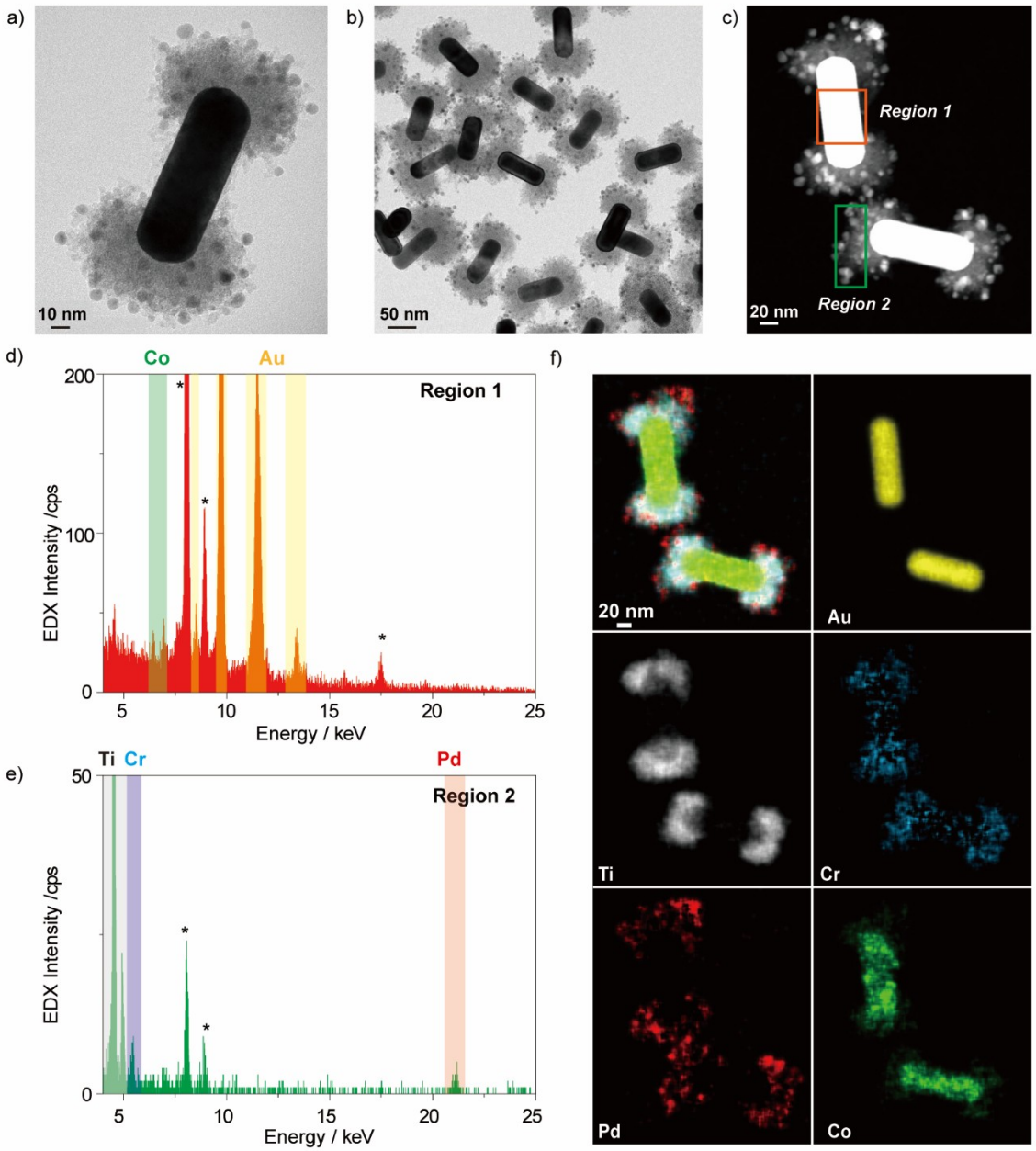

Figure 2. a-b) TEM images of the photocatalyst nanoparticles. **c-e)** HAADF-STEM image (c) and EDX spectra of the cap region (d, orange) and the central region 2 (e, green). * denotes Mo and Cu signals from background. **f)** STEM-EDX maps of Au-Lα, Ti-Kα, Pd-Lα, Co-Kα, and Cr-Kα lines.

Photocatalytic measurements were performed using a xenon lamp with a 400 nm long-pass filter to simulate AM 1.5G solar irradiation. The filter excluded the excitation of TiO_2. The oxygen evolution rate of the nanoparticles dispersed in 0.1 M potassium borate buffer (pH = 9.5) was quantified *in situ* by a calibrated Clark electrode.[43–45] No sacrificial reagents were added. The solution was purged rigorously with argon prior to measurements. Upon irradiation, the Clark electrode started to reduce the generated O_2. The O_2 concentration in solution was proportional to the electrical current of reduction. The current eventually reached a steady-state (plateau in Fig. 3a) level as the O_2

generation rate equaled the consumption rate. The higher the O_2 evolution rate, the higher the concentration plateau would become. The steady-state condition was used to calculate the O_2 evolution rate (Fig. S9). The integrated photocatalyst did not change its structure during the photocatalytic tests

(Fig. S11).

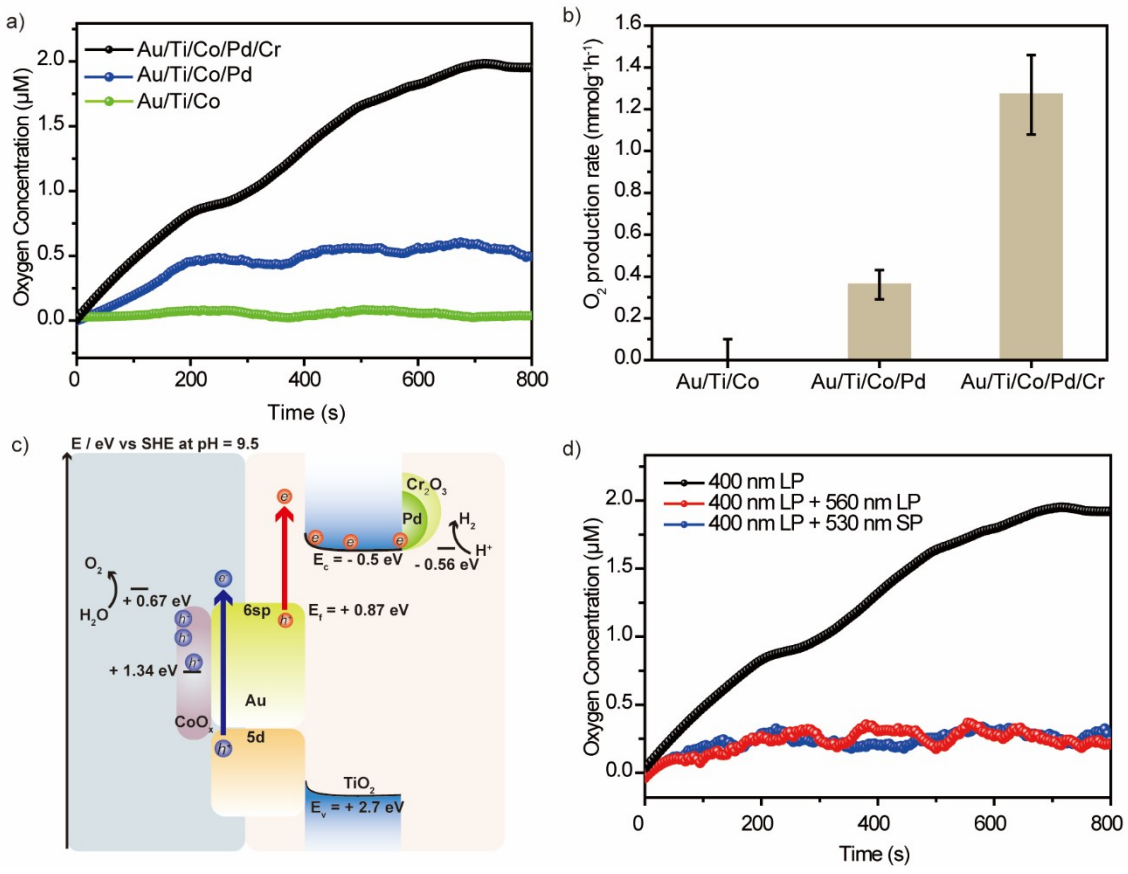
a)
Au/Ti/Co/Pd/Cr
Au/Ti/Co/Pd
Au/Ti/Co
Oxygen Concentration (μM)
Time (s)
b)
O2 production rate (mmolg-1h-1)
Au/Ti/Co
Au/Ti/Co/Pd
Au/Ti/Co/Pd/Cr
c)
E / eV vs SHE at pH = 9.5
O2
H2O
+ 0.67 eV
+ 1.34 eV
CoOx
6sp
Au
5d
Ef = + 0.87 eV
Cr2O3
Pd
H2
H+
Ec = - 0.5 eV
- 0.56 eV
TiO2
Ev = + 2.7 eV
d)
400 nm LP
400 nm LP + 560 nm LP
400 nm LP + 530 nm SP
Oxygen Concentration (μM)
Time (s)

Figure 3. a) Photocatalytic performance monitored via *in-situ* oxygen concentration measurements when no redox scavengers were added. **b)** Comparison of the O_2 evolution rate by various nanostructures. **c)** The proposed working principle of the photocatalyst utilizing carriers generated from both the interband and longitudinal LSPR transitions. **d)** The photocatalytic performance with different optical filters applied.

The performance of the integrated photocatalyst was compared with that of its precursors missing individual elements, and clearly demonstrated the necessity of incorporating all five components, each in their required position relative to the others (Fig. 3a and 3b). The O_2 evolution by $Au/TiO_2/CoO_x$ nanostructure was negligible due to the lack of HER sites. The deposition of cobalt oxide drastically improved the OER performance (Fig. S8), but HER activity is still required to balance the full redox cycle since no redox scavenger was added to the solution. With Pd incorporated, the O_2 evolution rate of $Au/TiO_2/CoO_x/Pd$ nanostructure reached 0.36 $mmolg^{-1}h^{-1}$. Furthermore, the full structure with Cr_2O_3 showed a much higher O_2 evolution rate at 1.27 $mmolg^{-1}h^{-1}$. The fact that the Cr_2O_3 thin layer greatly improved the O_2 evolution rate suggests that back reaction of O_2 on Pd surfaces was an efficiency-limiting factor. Similar effects were previously reported similar effects of Cr_2O_3 layer deposited onto noble metals.[35–37] The Cr_2O_3 layer is permeable to water, hydrated protons, and H_2, but blocks O_2. The possibility of back reaction was not surprising since HER and OER sites in our nanostructured photocatalyst were only separated by tens of nm. The higher photocatalytic activity of the fully integrated structure, as compared to its precursor structures with missing components, was also confirmed by measuring the HER activity using gas chromatography methods (Fig. S13). The pure oxygen production rate calculated from the Clark electrode measurements was about 10^{-11} $mol \cdot s^{-1}$, and the upper boundary for the rate of photo absorption was 3.26×10^{-7} einstein s^{-1}. Under the Z-scheme mechanism, the lower boundary of the apparent quantum yield for oxygen generation, defined as $2 \times (4 \times$ rate of O_2 generation$)$ / (rate of photon absorption), was calculated as 0.024%.[46] The OER quantum efficiency of the Au-based system here is lower than the reported values of semiconductor-based nanosystems. For instance, a Pt/CdS nanorod system with molecular OER catalysts loaded on the lateral sites were reported to split water with a quantum efficiency of 0.27% and a O_2 evolution rate per unit mass of 0.17 $mmolg^{-1}h^{-1}$.[14] The relatively lower efficiency of Au-based system could be due to the fast cooling rates of hot carriers before they are transferred to catalytic sites. However, the OER

rate per unit mass of the Au-based system is relatively high as a result of the large extinction coefficients of the LSPR and interband transitions of Au.

The proposed energy diagrams for the integrated photocatalyst is depicted in Fig. 3c. The hot electron generated from the LSPR transition has the suitable energy to cross the Schottky barrier and drives HER; the hot hole deep in the *d* band generated from the *d-sp* interband transition has the suitable energy to transfer to CoO_x and drives OER. The red arrow in Fig. 3c corresponds to the LSPR excitation generating a hot electron flowing across the Schottky barrier and a hole at the Fermi level of Au. The Fermi level of Au located at +0.87 eV is not energetic enough to drive OER on CoO_x.[47,48] The *d-sp* interband transition associated with the blue arrow promotes an electron from the *d* band of Au to its Fermi level, forming a hot hole in the *d* band.[3,4,32] The electron at the Au Fermi level does not have enough energy to cross the Schottky barrier at the Au/TiO_2 interface, whereas a fraction of the hot hole deep in the *d* band can be extracted to CoO_x to drive OER before cooling to the Fermi level.[3,49] When no scavengers were added to the photocatalytic test solution, oxygen evolution is only possible with hydrogen evolution to balance the redox cycle. Therefore, based on these energy diagrams, both the hot carriers derived from the LSPR transition and the interband transition are necessary for an Au NR absorber to account for the OER activity in Fig. 3a.

To verify the proposed charge transfer pathway in Fig. 3c, we applied optical filters and compared the photocatalytic performance to the white light excitation condition. When a 400 nm long-pass and a 560 nm long-pass filters were combined, we excited mostly the longitudinal LSPR mode with some contribution from the *d-sp* interband transition. When a 400 nm long-pass and a 530 nm short-pass filters were combined, we excited the *d-sp* interband transition and the transverse LSPR mode. The lamp intensity was adjusted to account for the optical loss of filters and maintain the spectral density of different excitation wavelengths at the AM 1.5G level with different filter sets. As shown in Fig. 3d, without any redox scavenger added, no oxygen production was observed when either the 560 nm long pass filter or the 530 nm short pass filter was applied. Oxygen evolution occurs readily when only the 400 nm long pass filter was applied. The data in Fig. 3d is consistent with the

mechanism that the longitudinal LSPR and the interband transition are each largely responsible for a half-reaction, and the full water splitting reaction could not proceed when either of the half-reactions was turned off. The lack of OER activity with the 530 nm short pass filter also suggests that the transverse LSPR mode is inefficient at promoting hot electrons across the Schottky barriers, because the hot electrons derived from the transverse LSPR mode mostly localizes at the lateral site of Au NR. To consolidate the proposed charge transfer mechanism, HER activity was also demonstrated to require the excitation of both the LSPR and interband transitions so that the full redox reaction can be balanced without scavengers (Fig. S13).

It has been demonstrated previously that the LSPR transitions alone can drive the HER half reaction in Au/TiO_2 Schottky junctions when hole scavengers are present.[22–24] When the electron scavenger potassium persulfate was added, we further demonstrate that the excitation with the 530 nm short pass filter alone can account for nearly all the OER activity of white light excitation, while the excitation with the 560 nm long pass filter generates negligible OER activity (Fig. S12). Unlike the case for HER, electrons at the Fermi level of Au have enough potential to reduce the persulfate anions. Therefore, exciting the interband transition alone should be sufficient to produce oxygen with persulfate present. Though the excitation conditions with long or short pass filters cannot absolutely separate out the interband and LSPR transitions,[40,50] the clear absence of OER activity when applying the 560 nm long pass filter suggests that the longitudinal LSPR mode does not contribute significantly to OER activity in the integrated photocatalyst.

It is rare for a single optical absorption band to possess the suitable energy levels to drive both the HER and OER while covering well the solar wavelength range.[51] Natural and artificial photosynthetic systems often contain multiple absorbers in the HER and OER units working in tandem to drive the overall reaction. Our results here suggest that the charge carriers generated from the longitudinal LSPR and the interband transitions in the same nanoparticle work in tandem to achieve a full water splitting reaction. This mechanism does not imply that the photocatalyst requires a simultaneous two-photon absorption exciting both the longitudinal LSPR and interband transitions to

function. The charge carriers from different transitions can flow tandemly as long as the charge separation lifetime is sufficiently long to accumulate charges between sequential photoexcitation events.[46] For future work, transient absorption measurements could be carried out to directly track the charge transfer pathway in the integrated system. The multiple interfaces between different material components could potentially generate charge trapping sites which are not well characterized within the scope of this work. Improved junction designs at the Au/CoO_x and Au/TiO_2 interfaces could be crucial for further enhancing the hot carrier harvesting efficiency. The solution phase photoredox deposition strategy demonstrated here can be used to precisely fabricate complex inorganic colloidal building blocks and assemblies with potential applications in energy harvesting, catalysis, plasmonics, and nanoelectronics.

Associated Content

The following files are available free of charge. Synthesis procedures, TEM and UV-vis characterizations, Details on electrochemical and photocatalytic tests (PDF)

Acknowledgement

This work was supported by the U.S. Department of Energy, Office of Science, Office of Basic Energy Sciences, Materials Sciences and Engineering Division, under Contract No. DE-AC02-05-CH11231 within the Characterization of Functional Nanomachines Program (KC1203). G.K and H.F. were supported by the Director, Office of Science, Office of Basic Energy Sciences, Division of Chemical, Geological and Biosciences of the U.S. Department of Energy under Contract No. DE-AC02-05CH11231. H.D.H. thanks the Samsung Scholarship for a graduate fellowship. STEM-EDX mapping work at the Molecular Foundry was supported by the Office of Science, Office of Basic Energy Sciences, of the U.S. Department of Energy under Contract No. DE-AC02-05-CH11231. The authors

appreciate Dr. Wojciech T. Osowiecki and Dr. Karen Bustillo for their discussion with STEM-EDX, as well as Dr. Yi-Yu Cai, Dr. Syed Mubeen and Dr. Martin Moskovits for their insightful discussions.

References

(1) Lewis, N. S.; Nocera, D. G. Powering the Planet: Chemical Challenges in Solar Energy Utilization. *Proc. Natl. Acad. Sci. U. S. A.* **2006**, *103* (43), 15729–15735.

(2) Davis, S. J.; Lewis, N. S.; Shaner, M.; Aggarwal, S.; Arent, D.; Azevedo, I. L.; Benson, S. M.; Bradley, T.; Brouwer, J.; Chiang, Y. M.; Clack, C. T. M.; Cohen, A.; Doig, S.; Edmonds, J.; Fennell, P.; Field, C. B.; Hannegan, B.; Hodge, B. M.; Hoffert, M. I.; Ingersoll, E.; Jaramillo, P.; Lackner, K. S.; Mach, K. J.; Mastrandrea, M.; Ogden, J.; Peterson, P. F.; Sanchez, D. L.; Sperling, D.; Stagner, J.; Trancik, J. E.; Yang, C. J.; Caldeira, K. Net-Zero Emissions Energy Systems. *Science* **2018**, *360* (6396), eaas9793.

(3) Mubeen, S.; Lee, J.; Singh, N.; Krämer, S.; Stucky, G. D.; Moskovits, M. An Autonomous Photosynthetic Device in Which All Charge Carriers Derive from Surface Plasmons. *Nat. Nanotechnol.* **2013**, *8* (4), 247–251.

(4) Duchene, J. S.; Tagliabue, G.; Welch, A. J.; Cheng, W. H.; Atwater, H. A. Hot Hole Collection and Photoelectrochemical CO_2 Reduction with Plasmonic Au/p-GaN Photocathodes. *Nano Lett.* **2018**, *18* (4), 2545–2550.

(5) Edri, E.; Cooper, J. K.; Sharp, I. D.; Guldi, D. M.; Frei, H. Ultrafast Charge Transfer between Light Absorber and Co_3O_4 Water Oxidation Catalyst across Molecular Wires Embedded in Silica Membrane. *J. Am. Chem. Soc.* **2017**, *139* (15), 5458–5466.

(6) Liu, C.; Tang, J.; Chen, H. M.; Liu, B.; Yang, P. A Fully Integrated Nanosystem of Semiconductor Nanowires for Direct Solar Water Splitting. *Nano Lett.* **2013**, *13* (6), 2989–2992.

(7) Jiang, C.; Moniz, S. J. A.; Wang, A.; Zhang, T.; Tang, J. Photoelectrochemical Devices for Solar Water Splitting-Materials and Challenges. *Chem. Soc. Rev.* **2017**, *46* (15), 4645–4660.

(8) Croce, R.; Van Amerongen, H. Natural Strategies for Photosynthetic Light Harvesting. *Nat. Chem. Biol.* **2014**, *10* (7), 492–501.

(9) Zhang, J. Z.; Reisner, E. Advancing Photosystem II Photoelectrochemistry for Semi-Artificial Photosynthesis. *Nat. Rev. Chem.* **2020**, *4* (1), 6–21.

(10) Cestellos-Blanco, S.; Zhang, H.; Kim, J. M.; Shen, Y. xiao; Yang, P. Photosynthetic Semiconductor Biohybrids for Solar-Driven Biocatalysis. *Nat. Catal.* **2020**, *3* (3), 245–255.

(11) Chen, P. C.; Liu, M.; Du, J. S.; Meckes, B.; Wang, S.; Lin, H.; Dravid, V. P.; Wolverton, C.; Mirkin, C. A. Interface and Heterostructure Design in Polyelemental Nanoparticles. *Science* **2019**, *363* (6430), 959–964.

(12) Steimle, B. C.; Fenton, J. L.; Schaak, R. E. Rational Construction of a Scalable Heterostructured Nanorod Megalibrary. *Science* **2020**, *367* (6476), 418-424.

(13) Oh, M. H.; Cho, M. G.; Chung, D. Y.; Park, I.; Kwon, Y. P.; Ophus, C.; Kim, D.; Kim, M. G.; Jeong, B.; Gu, X. W.; Jo, J.; Yoo, J. M.; Hong, J.; McMains, S.; Kang, K.; Sung, Y. E.; Alivisatos, A. P.; Hyeon, T. Design and Synthesis of Multigrain Nanocrystals via Geometric Misfit Strain. *Nature* **2020**, *577* (7790), 359–363.

(14) Wolff, C. M.; Frischmann, P. D.; Schulze, M.; Bohn, B. J.; Wein, R.; Livadas, P.; Carlson, M. T.; Jäckel, F.; Feldmann, J.; Würthner, F.; Stolarczyk, J. K. All-in-One Visible-Light-Driven Water Splitting by Combining Nanoparticulate and Molecular Co-Catalysts on CdS Nanorods. *Nat. Energy* **2018**, *3* (10), 862–869.

(15) Kalisman, P.; Nakibli, Y.; Amirav, L. Perfect Photon-to-Hydrogen Conversion Efficiency. *Nano Lett.* **2016**, *16* (3), 1776–1781.

(16) Zhu, M.; Wang, Y.; Deng, Y. H.; Peng, X.; Wang, X.; Yuan, H.; Yang, Z. J.; Wang, Y.; Wang, H. Strategic Modulation of Energy Transfer in Au-TiO_2-Pt Nanodumbbells: Plasmon-Enhanced Hydrogen Evolution Reaction. *Nanoscale* **2020**, *12* (13), 7035–7044.

(17) Zheng, Z.; Tachikawa, T.; Majima, T. Single-Particle Study of Pt-Modified Au Nanorods for Plasmon-Enhanced Hydrogen Generation in Visible to near-Infrared Region. *J. Am. Chem. Soc.* **2014**, *136* (19), 6870–6873.

(18) Kalisman, P.; Kauffmann, Y.; Amirav, L. Photochemical Oxidation on Nanorod Photocatalysts. *J. Mater. Chem. A* **2015**, *3* (7), 3261–3265.

(19) Dukovic, G.; Merkle, M. G.; Nelson, J. H.; Hughes, S. M.; Alivisatos, A. P. Photodeposition of Pt on Colloidal CdS and CdSe/CdS Semiconductor Nanostructures. *Adv. Mater.* **2008**, *20* (22), 4306–4311.

(20) Ben-Shahar, Y.; Scotognella, F.; Kriegel, I.; Moretti, L.; Cerullo, G.; Rabani, E.; Banin, U. Optimal Metal Domain Size for Photocatalysis with Hybrid Semiconductor-Metal Nanorods. *Nat. Commun.* **2016**, *7*, 1–7.

(21) Wu, B.; Liu, D.; Mubeen, S.; Chuong, T. T.; Moskovits, M.; Stucky, G. D. Anisotropic Growth of TiO2 onto Gold Nanorods for Plasmon-Enhanced Hydrogen Production from Water Reduction. *J. Am. Chem. Soc.* **2016**, *138* (4), 1114–1117.

(22) Duchene, J. S.; Sweeny, B. C.; Johnston-Peck, A. C.; Su, D.; Stach, E. A.; Wei, W. D. Prolonged Hot Electron Dynamics in Plasmonic-Metal/Semiconductor Heterostructures with Implications for Solar Photocatalysis. *Angew. Chemie - Int. Ed.* **2014**, *53* (30), 7887–7891.

(23) Qian, K.; Sweeny, B. C.; Johnston-Peck, A. C.; Niu, W.; Graham, J. O.; Duchene, J. S.; Qiu, J.; Wang, Y. C.; Engelhard, M. H.; Su, D.; Stach, E. A.; Wei, W. D. Surface Plasmon-Driven Water Reduction: Gold Nanoparticle Size Matters. *J. Am. Chem. Soc.* **2014**, *136* (28), 9842–9845.

(24) Elbanna, O.; Kim, S.; Fujitsuka, M.; Majima, T. TiO_2 Mesocrystals Composited with Gold Nanorods for Highly Efficient Visible-NIR-Photocatalytic Hydrogen Production. *Nano Energy* **2017**, *35*, 1–8.

(25) Winsemius, P.; Guerrisi, M.; Rosei, R. Splitting of the Interband Absorption Edge in Au: Temperature Dependence. *Phys. Rev. B* **1975**, *12* (10), 4570–4572.

(26) Halas, N. J.; Lal, S.; Chang, W. S.; Link, S.; Nordlander, P. Plasmons in Strongly Coupled Metallic Nanostructures. *Chem. Rev.* **2011**, *111* (6), 3913–3961.

(27) Brongersma, M. L.; Halas, N. J.; Nordlander, P. Plasmon-Induced Hot Carrier Science and Technology. *Nat. Nanotechnol.* **2015**, *10* (1), 25–34.

(28) Ye, X.; Zheng, C.; Chen, J.; Gao, Y.; Murray, C. B. Using Binary Surfactant Mixtures to Simultaneously Improve the Dimensional Tunability and Monodispersity in the Seeded Growth of Gold Nanorods. *Nano Lett.* **2013**, *13* (2), 765–771.

(29) Kim, Y.; Smith, J. G.; Jain, P. K. Harvesting Multiple Electron-Hole Pairs Generated through Plasmonic Excitation of Au Nanoparticles. *Nat. Chem.* **2018**, *10* (7), 763–769.

(30) Zhao, J.; Nguyen, S. C.; Ye, R.; Ye, B.; Weller, H.; Somorjai, G. A.; Alivisatos, A. P.; Dean Toste, F. A Comparison of Photocatalytic Activities of Gold Nanoparticles Following Plasmonic and Interband Excitation and a Strategy for Harnessing Interband Hot Carriers for Solution Phase Photocatalysis. *ACS Cent. Sci.* **2017**, *3* (5), 482–488.

(31) Zou, N.; Chen, G.; Mao, X.; Shen, H.; Choudhary, E.; Zhou, X.; Chen, P. Imaging Catalytic Hotspots on Single Plasmonic Nanostructures via Correlated Super-Resolution and Electron Microscopy. *ACS Nano* **2018**, *12* (6), 5570–5579.

(32) Bernardi, M.; Mustafa, J.; Neaton, J. B.; Louie, S. G. Theory and Computation of Hot Carriers Generated by Surface Plasmon Polaritons in Noble Metals. *Nat. Commun.* **2015**, *6*, Article number: 7044.

(33) Ding, D.; Liu, K.; He, S.; Gao, C.; Yin, Y. Ligand-Exchange Assisted Formation of Au/TiO_2 Schottky Contact for Visible-Light Photocatalysis. *Nano Lett.* **2014**, *14* (11), 6731–6736.

(34) Knight, M. W.; Sobhani, H.; Nordlander, P.; Halas, N. J. Photodetection with Active Optical Antennas. *Science* **2011**, *332* (6030), 702–704.

(35) Takata, T.; Jiang, J.; Sakata, Y.; Nakabayashi, M.; Shibata, N.; Nandal, V.; Seki, K.; Hisatomi, T.; Domen, K. Photocatalytic Water Splitting with a Quantum Efficiency of Almost Unity. *Nature* **2020**, *581* (7809), 411–414.

(36) Maeda, K.; Teramura, K.; Lu, D.; Saito, N.; Inoue, Y.; Domen, K. Noble-Metal/Cr_2O_3 Core/Shell Nanoparticles as a Cocatalyst for Photocatalytic Overall Water Splitting. *Angew. Chemie - Int. Ed.* **2006**, *45* (46), 7806–7809.

(37) Yoshida, M.; Takanabe, K.; Maeda, K.; Ishikawa, A.; Kubota, J.; Sakata, Y.; Ikezawa, Y.; Domen, K. Role and Function of Noble-Metal/Cr-Layer Core/Shell Structure Cocatalysts for

Photocatalytic Overall Water Splitting Studied by Model Electrodes. *J. Phys. Chem. C* **2009**, *113* (23), 10151–10157.

(38) Nishi, H.; Tatsuma, T. Mechanistic Analysis of Plasmon-Induced Charge Separation by the Use of Chemically Synthesized Gold Nanorods. *J. Phys. Chem. C* **2018**, *122* (4), 2330–2335.

(39) Zuloaga, J.; Prodan, E.; Nordlander, P. Quantum Plasmonics: Optical Properties and Tunability of Metallic Nanorods. *ACS Nano* **2010**, *4* (9), 5269–5276. https://doi.org/10.1021/nn101589n.

(40) Mills, H. N. Optical properties of chalcogenide glasses. *J. Non. Cryst. Solids* **1982**, *47* (1), 27–46.

(41) Beversluis, M.; Bouhelier, A.; Novotny, L. Continuum Generation from Single Gold Nanostructures through Near-Field Mediated Intraband Transitions. *Phys. Rev. B - Condens. Matter Mater. Phys.* **2003**, *68* (11), 1–10.

(42) Schoenlein, R. W.; Lin, W. Z.; Fujimoto, J. G.; Eesley, G. L. Femtosecond Studies of Nonequilibrium Electronic Processes in Metals. *Phys. Rev. Lett.* **1987**, *58* (16), 1680–1683.

(43) Li, J. X.; Ye, C.; Li, X. B.; Li, Z. J.; Gao, X. W.; Chen, B.; Tung, C. H.; Wu, L. Z. A Redox Shuttle Accelerates O_2 Evolution of Photocatalysts Formed In Situ under Visible Light. *Adv. Mater.* **2017**, *29* (17), 2–7.

(44) Materna, K. L.; Jiang, J.; Regan, K. P.; Schmuttenmaer, C. A.; Crabtree, R. H.; Brudvig, G. W. Optimization of Photoanodes for Photocatalytic Water Oxidation by Combining a Heterogenized Iridium Water-Oxidation Catalyst with a High-Potential Porphyrin Photosensitizer. *ChemSusChem* **2017**, *10* (22), 4526–4534.

(45) Liu, H.; Frei, H. Observation of O-O Bond Forming Step of Molecular Co_4O_4 Cubane Catalyst for Water Oxidation by Rapid-Scan FT-IR Spectroscopy. *ACS Catal.* **2020**, *10* (3), 2138–2147.

(46) Wang, Q.; Hisatomi, T.; Ma, S. S. K.; Li, Y.; Domen, K. Core/Shell Structured La- and Rh-Codoped $SrTiO_3$ as a Hydrogen Evolution Photocatalyst in Z-Scheme Overall Water Splitting under Visible Light Irradiation. *Chem. Mater.* **2014**, *26* (14), 4144–4150.

(47) Hou, W.; Cronin, S. B. A Review of Surface Plasmon Resonance-Enhanced Photocatalysis. *Adv. Funct. Mater.* **2013**, *23* (13), 1612–1619.

(48) Tachikawa, T.; Zhang, P.; Bian, Z.; Majima, T. Efficient Charge Separation and Photooxidation on Cobalt Phosphate-Loaded TiO_2 Mesocrystal Superstructures. *J. Mater. Chem. A* **2014**, *2* (10), 3381–3388.

(49) Lee, J.; Mubeen, S.; Ji, X.; Stucky, G. D.; Moskovits, M. Plasmonic Photoanodes for Solar Water Splitting with Visible Light. *Nano Lett.* **2012**, *12* (9), 5014–5019.

(50) Brown, A. M.; Sundararaman, R.; Narang, P.; Goddard, W. A.; Atwater, H. A. Nonradiative Plasmon Decay and Hot Carrier Dynamics: Effects of Phonons, Surfaces, and Geometry. *ACS Nano* **2016**, *10* (1), 957–966.

(51) Ng, B. J.; Putri, L. K.; Kong, X. Y.; Teh, Y. W.; Pasbakhsh, P.; Chai, S. P. Z-Scheme Photocatalytic Systems for Solar Water Splitting. *Adv. Sci.* **2020**, *1903171*.

(52) Xia, X.; Song, M.; Wang, H.; Zhang, X.; Sui, N.; Zhang, Q.; Colvin, V. L.; Yu, W. W. Latest Progress in Constructing Solid-State Z Scheme Photocatalysts for Water Splitting. *Nanoscale* **2019**, *11* (23), 11071–11082.

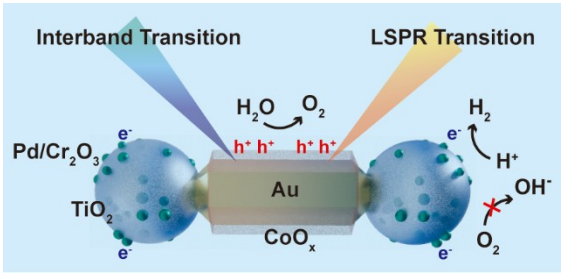

For Table of Contents Only